Validating Surface Evolution Modeling on High Temperature Selective Emitters: An Investigation of the Thermal Stability of Nano-Scale Surface Structures for Thermophotovoltaic Systems

by
Sun K. Kim

Submitted to the Department of Mechanical Engineering
In partial fulfillment of the Requirements for the Degree of

Bachelor of Science in Mechanical Engineering
At the
Massachusetts Institute of Technology
June 2011

Signature of Author: _____
Department of Mechanical Engineering
May 6, 2011

Certified by: _____
Sang-Gook Kim
Professor of Mechanical Engineering
Thesis Supervisor

Accepted by: _____
John H. Lienhard V
Collins Professor of Mechanical Engineering
Chairman, Undergraduate Thesis Committee

[This page is intentionally left blank.]

Validating Surface Evolution Modeling on High Temperature Selective Emitters: An Investigation of the Thermal Stability of Nano-Scale Surface Structures for Thermophotovoltaic Systems

by

Sun K. Kim

Submitted to the Department of Mechanical Engineering in partial fulfillment of the Requirements for the Degree of Bachelor of Science in Mechanical Engineering

ABSTRACT

As the world's traditional energy sources come under scrutiny due to dwindling supply and negative environmental impact, a global effort is being made into alternative energy systems. One such system involves the use of thermophotovoltaics (TPV), which convert thermal energy to electricity. Nano-patterned features can improve electromagnetic emission from the TPV emitter, increasing system efficiency. These features, however, degrade at high temperatures over time. One of the main contributors to surface evolution is surface diffusion. This investigation tested surface diffusion based simulation modeling, comparing computational results with experimental findings for high temperature annealed silicon, a cost effective material for testing instead of tungsten. Although the simulation model fits within 25% of the post-annealed curvature caused by surface diffusion, discrepancies in the simulation's time scale need to be addressed in future models for accurate time dependent modeling.

Thesis Supervisor: Sang-Gook Kim

Title: MIT Professor of Mechanical Engineering

Acknowledgements

I would like to thank my thesis supervisor Professor Sang-Gook Kim for advising me of the guidelines and content necessary for this undergraduate thesis. He has been extremely helpful with me during this entire endeavor, dating back to an undergraduate research opportunity program in the Fall of 2010 and has inspired me to pursue the frontiers of research. I would also like to thank doctoral candidate Stephen Bathurst for his patience and wisdom in familiarizing me with the research at hand, serving as the foundation of this thesis. Gratitude to doctoral candidate Heon-Ju Lee is also warranted for his guidance. Finally, I would like to thank Kurt Broderick of the MTL for his help and patience during high temperature annealing and contact profilometry.

Table of Contents

List of Figures

List of Tables

List of Symbols

Symbol	Definition
E	Energy
h	Planck's constant
f	Frequency
c	Speed of light
λ	Wavelength
M	Magnitude of magnetic field
eV	Electron volt

V_n	Velocity normal to surface
A	Vapor transport constant
Ω	Volume per atom
γ	Surface free energy per area
P^{eq}	Vapor pressure in equilibrium with a local region of the surface with zero curvature
κ	Curvature
T	Temperature
k	Boltzmann's constant
D_v	Volumetric diffusion constant
D_s	Surface diffusion constant
R	Radius
λ	Linear dimension

Chapter 1. Thesis Objective

In September 2006, the MIT Energy Initiative (MITEI) chartered to "transform the global energy system to meet the needs of the future and to help bridge that future by improving today's energy systems." The need for new supplies of affordable, sustainable energy for the world is very clear, providing one of the greatest global challenges of the 21st century. According to the Report of the Energy Research Council, the foundation of the 2006 MIT Energy Initiative, a convergence is on the horizon for a "perfect storm" of issues associated with energy: supply and demand, security, and environmental impacts. Energy demand is expected to far outpace energy supply in the next fifty years, with some estimates predicting doubling of energy use and tripling of electricity demand, most of which requiring fossil fuel and carbon based energy sources. The geopolitical climate, in the Middle East particularly, remains unstable (made evident in the recent governmental upheavals in Egypt, Yemen, Libya, etc.) and jeopardizes the availability of fossil fuel energy sources. Finally, the magnitude of greenhouse emissions from carbon-based combustion, although hotly debated in political forums, cannot be ignored. Policy should seek to lower carbon intensities, improve efficiencies, and develop comprehensive sequestration systems.

The MITEI hopes to inspire and invigorate important research and policy that will serve as the foundation for an energy transition into the century, including renewable energy, energy storage and conversion, interdisciplinary collaboration, enhanced dependability of energy systems, climate change, and increased energy efficiency. Much work in solar power, nuclear systems, and integrated technology and climate change policy serves as an initial charge into the prescribed goals [1].

Significant breakthroughs are required for solar technologies to achieve the greatest energy goals. A large obstacle is the prohibitive costs of developing these technologies with

high enough efficiency for practical use. Manufacturing process technologies need to reduce costs and improve performance in the near future. Other avenues of research include the exploration of inorganic, organic, and photobiological photovoltaics. The purpose of this undergraduate thesis is to promote the work of tungsten emitter surfaces for thermophotovoltaic applications. Creating viable thermophotovoltaic systems would change the field of solar energy with the development of efficient, low cost, and scalable solar to thermal then to electrical conversion technologies. Thermophotovoltaics convert heat to electrical energy and are usually comprised of emitters, spectral control components, and photovoltaic diodes. Their efficiency can be increased by having a nano-structured photonic crystal operated at high (>1000 ^{o}C) temperatures for spectral control. A good selective emitter should exhibit low emissivity for photonics with energies below the PV band gap and high emissivity for photons with higher energies. However, an obstacle TPV faces at high temperatures is thermal deterioration of the nano-patterned emitter surface from several factors – recrystallization, surface diffusion, bulk/volume diffusion, and vapor pressure driven evaporation and condensation. In fact, no nano-structures have been developed for high temperature uses. It is hypothesized that surface diffusion is the main source of surface deterioration. In previous research at the Micro/Nano Systems Laboratory headed by Professor Sang-Gook Kim, a 10 nm thin film of Titanium Nitride formed an interface layer of TiON through oxygen stuffing, implanting oxygen molecules at the grain boundaries through oxygen plasma treatment. This multi-layered stack provided promising diffusion barrier performance. The prototyped fabrication of the 1D photonic crystal is currently under development. The work presented here will analyze experimental silicon samples operated at 1000° C for different durations and compare the micro-patterned surface features with simulation models in an effort to validate the current simulation models for surface diffusion. SEM imaging and contact profilometry are

used to characterize the surface features of the experimental silicon samples. Silicon substrates were used for their economical cost, prevalent use, well-documented phenomena at high temperature operations for semiconductor technologies.

Chapter 2. Thermophotovoltaics

Section 2.1. Introduction

Creating viable thermophotovoltaic (TPV) systems would change the field of solar energy with the development of efficient, low cost, and scalable solar to thermal then to electrical conversion technologies. Thermophotovoltaics convert heat to electrical energy and are usually comprised of emitters, spectral control components, and photovoltaic diodes. Their efficiency can be increased by having a nano-structured emitter which should be operated at high (>1000 ^{o}C) temperatures for spectral control. However, one major obstacle TPV faces is thermal deterioration of the nano-patterned emitter surface at high temperatures. Even with the recent advancements in nanotechnology and material science, no nanostructures have been used at these extremely high operation temperatures.

Although tungsten is a suitable material for its high melting point and high thermal stability with its low evaporation rate in vacuums, nano-patterned tungsten surfaces degrade considerably at 1000 ^{o}C or higher temperatures due to primary recrystallization and surface diffusion. Thermal degradation results from several factors – recrystallization, surface diffusion, bulk/volume diffusion, and vapor pressure driven evaporation and condensation. It is hypothesized that surface diffusion and recrystallization are the main sources of surface deterioration. In order to see the effect of surface diffusion decoupled from recrystallization, single crystal silicon is investigated in this thesis.

Section 2.2. The Electromagnetic Spectrum

It is important to begin a discussion on thermal energy conversion by providing a background on the electromagnetic spectrum. Photons, which make up electromagnetic

radiation, are the smallest units in the electromagnetic field. Photons can be produced in a number of ways: when a bound electron moves from one orbital to one of lesser energy, the byproduct of nuclear decay, accelerated charged particles, and atomic collisions. They exhibit a wave-particle duality: although massless, they have energy and momentum proportional to their frequency; they also have wavelengths and optical properties suggesting wave-like behavior. Photonic energy is given by the de Broglie wave relation,

$$E = hf = cp, f = \frac{c}{\lambda} \tag{1}$$

where h is Planck's constant ($6.626 \cdot 10^{-34}$ J·s), f is the frequency, c is the speed of light (3E8 m/s), λ is the wavelength, and p is the momentum. Figure 1 displays how a photon travels through space. When a single unbound electron passes through a one volt electrostatic potential difference in a vacuum, it gains one electron volt (eV) of kinetic energy, or $1.602 \cdot 10^{-19}$ J.

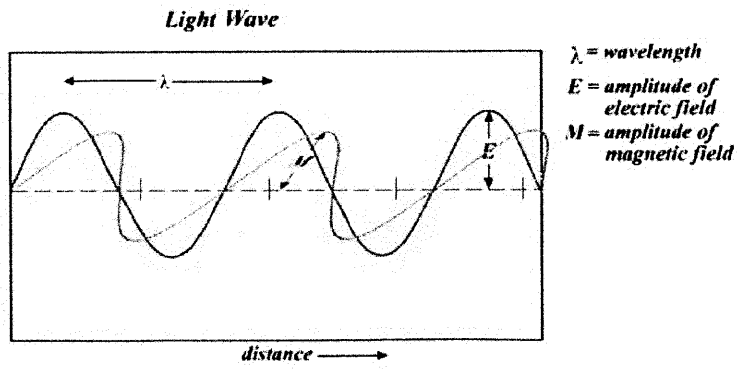

Figure 1: Electric and magnetic fields produced by moving photons [2].

The electromagnetic spectrum contains a wide range of wavelengths (and therefore frequencies) in which photons move through space. Figure 2 highlights the spectrum in terms of wavelength, nomenclatures, sources, and frequencies.

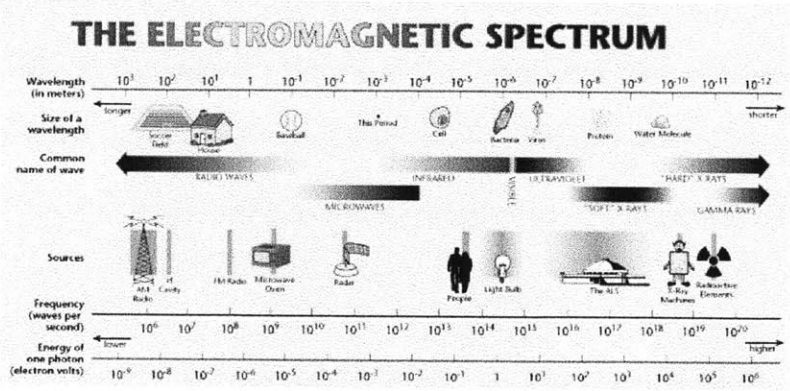

Figure 2: Electromagnetic spectrum [2].

The subject matter in this investigation focuses on infrared radiation, the energy associated with heat transfer and thermal energy. Wavelengths range from 750 nm to 1000 nm and have frequencies of 300 GHz to 400 THz. The corresponding energies range from 1.24 meV to 1.65 eV [2].

Section 2.3. History and Development

Thermoelectric , thermionic, and TPV research has created the development for static energy conversion to electricity, providing systems that have no mechanical losses, can be fabricated on the mico- and nano-scales, leading to the ability to design a compact, integrated, and robust system. Despite these strengths, proven applications for thermoelectric and thermoionic effects have been few and far between, with devices limited in efficiency (10% of theoretical maximum efficiency) or difficulties in lifespan and complexity of design for the systems.

In thermoelectric devices utilize thermally excited electrons that travel through a crystal lattice to create an electric current. Electron-phonon scattering allows electrons to exchange energy with the lattice from the hot to cold sides. Although electron sharing is a faster process than heat transfer, a good thermoelectric device should be made from a material that is a good electrical but poor thermal conductor. Despite research in materials known as clathrates, also known as cage compounds that contain a molecular lattice within another molecular lattice, more research is needed to approach higher levels of efficiency.

Thermionic devices include an emitter and a collector, in which the higher temperature emitter transmits electrons to the lower temperature collector. The electrons overcome the material potential barrier, or its work function, the minimum energy to eject an electron from a solid surface. Difficulties implementing this design include maintaining a high enough (greater than 1800°C) temperature while having electrical contact with the rest of the device and finding a robust enough material with a low work function.

Both of the preceding examples used a common medium for heat flow and electrical current, which leads to a difficult challenge to maintain a working configuration for long periods of time. TPV devices separates the heat source from the converter [3].

Although silicon solar cells and photovoltaic (PV) technology are well-known and commonly used to convert sunlight to electrical energy, thermophotovoltaic (TPV) systems provide a versatile approach to alternative energy. TPVs are not restricted to solar environments: they can be utilized in areas with ample radiant heat, such as metal foundries and combustion chambers [4]. TPV systems have a higher theoretical efficiency compared to traditional PV cells (85% vs. 32%) [5], can minimize pollutants and require little maintenance.
Thermophotovoltaics have their conceptual beginnings in a series of lectures by Pierre Aigrain

of the École Normale Supéreure in Paris, France. In late 1960 and early 1961, as a visiting professor at the Massachusetts Institute of Technology, Aigrain proposed a direct energy conversion concept a pursued extensive research in TPVs viability [6]. Also in the early 1960s, US army researchers, led by Dr. Emil Kittl and Dr. Guido Guazzoni, at Fort Monmouth, NJ developed the first documented TPV generator and also assisted in growing the field to universities and related industries. The energy crises of the 1970s spurred interest in alternative energy, with a particular emphasis on solar energy. The Electric Power Research Institute (EPRI), however, investigated the use of longer wavelengths characterized by thermophotovoltaic systems. Advancements, despite arriving at a steady pace, in TPV technologies have been hindered by the inability to identify low cost and scalable solutions. Thermophotovoltaic technology has manifested in promising applications in use today, such as the Western Washington University development of an electric hybrid vehicle that uses a TPV generator to produce 10 kW of power, harnessing waste heat in automobiles for thermophotovoltaic auxiliary power generation, and the creation of $CuInGaSe_2$ (CIGS) photocells for a novel thin film TPV system with appropriate band gap and low resistance. The main desire of this thesis is to assist in the arrival of the goal of the efficient, economical, and commoditization of TPV technologies [4,22-24].

Section 2.4. Heat Conversion to Electricity

Thermophotovoltaics convert radiant heat to electric energy, consisting of an emitter, a spectral control component, and a photovoltaic diode. The emitter is a solid material or a specifically engineered structure that radiates electromagnetic energy to the PV converter. The electromagnetic radiation associated with TPV systems is infrared energy, the bandwidth of radiation from 0.7 microns to 300 microns. The PV converter is only able to convert a specific

range of wavelengths within this electromagnetic spectrum. For solar applications, silicon PV cells should match the the AM1.5 (air mass coefficient associated with 1.5 atmosphere thickness) of the solar spectrum. However, as shown in Figure 3, there is much room for improvement to increase the available fraction for use in the solar spectrum [7].

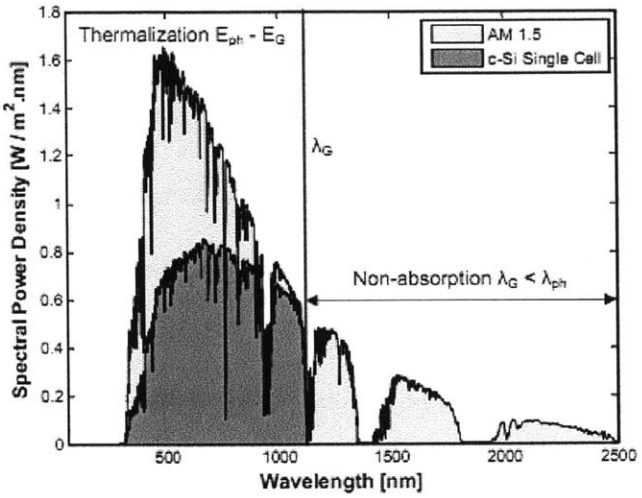

Figure 3: Fraction of the AM1.5 solar spectrum that can be converted by a silicon PV cell into usable energy [7].

An open flame, however, is not a suitable radiation source since the wavelengths and intensities vary over time. Therefore, the heat source must raise the emitter temperature to a specific range of temperatures (900°-1700° C). The emitter radiates a band of wavelengths which can be captured by the PV converter, whose properties depend on material and structure. Filters and selective emitters narrow the wavelength bandwidth to optimize the specific PV converter in the TPV system. Unused energy can be reflected back to the radiator to be recycled, depending on the geometric setup of the TPV system. Emitters are constructed on the basis of efficiency, temperature resistance, and cost. Figure 4 demonstrates this procedure.

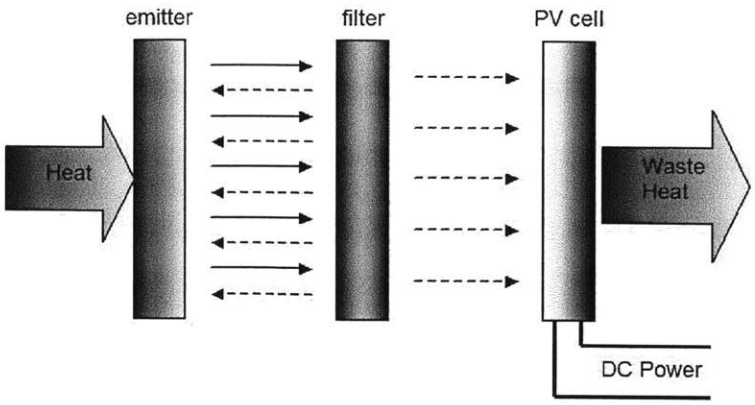

Figure 4: Schematic of emitter radiation [8].

The wavelengths emitted should correspond to the energy needed to free electrons from the valence band, the most energetic immobile electrons, to the conduction band, where electrons can flow in a current within the semiconductor converter. This energy is referred to as the band-gap energy, in which photons with enough energy to move an electron from the valence band to the conduction band. This phenomenon is referred to as the photovoltaic effect and is demonstrated commonly in semiconductor crystals in PV applications [4].

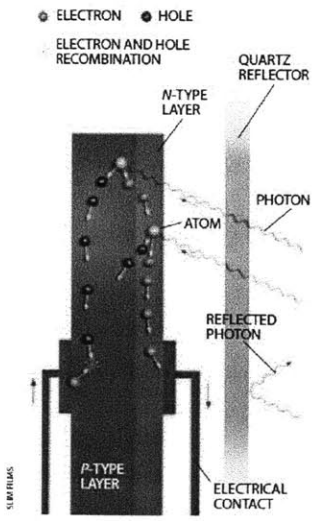

Figure 5: The Photovoltaic Effect [4].

In a semiconductor, electrons partially fill the conduction band, creating an initially negative charge. Vacant energy levels in the valence bands or holes create an initially positive charge. N-type semiconductors have more electrons in the conduction band than holes in the valence band, and P-type semiconductors have more holes in the valence band than electrons in the conduction band. The contact between N-type and P-type semiconductor materials creates a diode, resulting in a buildup of electrical potential, the aforementioned band gap. Photons with energy greater than or equal to the band gap cause electrons to jump the diode junction, altering the concentrations of electrons and holes. Electrons move to the n side of the junction and holes move to the p side, cascading to cause the photovoltaic effect, where technology harnesses that energy for external electrical circuitry. Photons with energy greater than the band gap generate heat with the excess energy, and photons with less than the band gap energy can be reflected by a reflector or simply not absorbed. The band gap varies on the type of semiconductor material used; typical values for solar cells are between 1.0 to 1.5 eV. For TPV cells, a 0.5 to 0.7 eV energy requirement is common, meaning that a lower photonic energy is required to induce an electrical current in a TPV system [4]. Figure 5 illustrates the photovoltaic effect.

The spectral emissivity of thermophotovoltaic emitters should match the bandgap of the photovoltaic cell. The emitter should be thermally stable, poorly emissive for energies lower than the bandgap energy of the PV cell, and highly emissive for energies higher than the bandgap. Spectral emissivity is oftentimes seen as a property of the radiating material. Radiation is related to the photonic density of states, or number of optical modes, the various excitations levels of atoms in a solid lattice. The number of optical modes can be increased by choosing a suitable material and physically constructing favorable geometries for spectral

emission. It has been shown that surface-relief gratings increase emissivity due to wave diffraction effects called Wood's anomalies. These structures are sensitive to surface diffusion, which can be countered with diffusion barriers such as hafnium oxide (explained in Chapter 3). This thesis will investigate thermal stability of these surface structures for TPV systems by validating simulation modeling of this phenomenon [9].

Section 2.5. Thermophotovoltaic System Components and Material Selection

Much of the current research on TPV technologies (including the focus of this study) encompasses emitter and PV converter materials. This study provides a basic overview of common materials:

2.5.1. Emitters

Silicon carbide (SiC) is the most common material used for TPV systems using an external burner. It is usually coupled with non-absorbing selective filters or mirrors to reflect longer wavelengths back to the emitter in order to recycle unconverted energy. Tungsten is the most common refractory metal for its low emissivity in mid to far IR bandwidth and its low evaporation rate in vacuums at high temperatures. This investigation complements the crystalline tungsten emitter work by doctorate students in the Micro/Nano Systems Laboratory at MIT. Erbium and ytterium oxides are used as selective emitters, although discrepancies between their emission peaks and conventional band gaps result in a sharp drop in efficiency. Finally, photonic crystals are engineered metals and semiconductor materials that specify emission and absorption properties, promoting a more effective design of selective emitters. These emitters, however, are restrictive in cost and development time due to their intensive manufacturing procedures [9]. Although this investigation uses silicon wafers to model surface

evolution, the main TPV research at the Micro/Nano Systems Laboratory uses tungsten photon crystals for the emitter.

2.5.2. Photovoltaic Converters

Although silicon is widely used in solar cell PV applications, no efficient Si PV converter has been created due to silicon's emitter limitations at lower operating temperatures. Gallium antimonide (GaSb) is commonly used in most PV cells due to its ease of manufacture and narrow band gap of 0.72 eV. Indium Gallium Arsenide Antimonide is expensive to implement and create complications in phase separation at high operating temperatures. Much of the current research is devoted to developments in III-V semiconductor compounds [10-11].

Chapter 3. Thermal Degradation Modes

At high operating temperatures that thermophotovoltaic systems operate, surface deformation phenomena are prevalent. In particular, recrystallization, evaporation and condensation, bulk volume diffusion, and surface diffusion have been identified as mechanisms for surface evolution [12]. The subsequent sections describe the mechanisms in detail[1].

Section 3.1. Recrystallization

Deformed grains, or microscopic crystals, within a material can reform to an energetically more stable grain structure in a process known as recrystallization, which is primarily driven by temperature. Once the critical recrystallization temperature is reached, nucleated grains along a grain boundary grow until the maximum grain size is achieved. This process can occur when there is stored energy within the structure, such as residual stress from deformation. Annealing relieves the residual stress, decreasing the strength and hardness and increasing the ductility of the material by minimizing recrystallization. In order to prevent surface features from destruction during this process, the emitter material may be pre-annealed to release the residual stresses in the structure and then patterned. Figure 6 illustrates recrystallization.

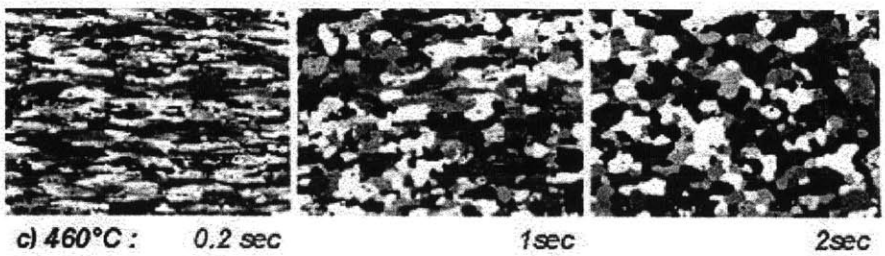

Figure 6: Annealing treatment of cold rolled aluminum demonstrating grain growth [13].

[1] It is assumed that plastic flow does not occur (that is, the operating temperatures are below the melting point).

Section 3.2. Evaporation and Condensation

Evaporation and condensation are mass transfer processes related to the local vapor pressure near the surface of the material, usually at high temperatures. The evaporation and deposition of material is proportional to the surface curvature and the material's ambient vapor pressure. The mechanism for shape morphology is dictated by the Gibbs-Thomson Effect, surface tension's effect on vapor pressure and chemical potential leading to changes in surface curvature. Mullins describes the normal velocity as:

$$V_n = -\frac{A\Omega^2 \gamma P^{eq}}{kT}\kappa = -A\kappa, \qquad (2)$$

where V_n is the velocity of the interface normal to the surface, A is a vapor transport rate constant, Ω is the volume per atom, γ is the interfacial free energy per area, P^{eq} is the vapor pressure in equilibrium with a local region of the surface with zero curvature, k is the Boltzmann constant, T the temperature and κ the local curvature [16].

Section 3.3. Bulk Volume and Surface Diffusion

Diffusion of atoms occurs readily at high temperatures and can cause shape transformation. Atoms move through a crystal lattice through mean free energy, which is primarily dictated by temperature. Atoms "jumping" to different sites within the lattice in the structure define volume diffusion (or bulk diffusion), while atoms jumping to different sites within the lattice on the surface define surface diffusion. Surface diffusion is related to adsorption, the adhesion of foreign particles to the surface. These particles form a film of adsorbate, usually through van der Waals or similar intermolecular forces. The surface of the adsorbent is no longer a surface and lowers to a more energetically favorable state [15] The

ratio of atoms moving on the surface to atoms moving within the material is approximately $R=D_s/D_v$, where D_s is the surface diffusion constant, D_v is the bulk diffusion constant, and w is the effective groove width. This width is on the nano-scale, indicating that surface diffusion dominates volume diffusion in most cases (typically on the order of 10^2) [16]. The value of volumetric diffusion is $1 \cdot 10^{-7}$ $\mu m^2/s$ at 1100 °C while surface diffusion during hydrogen annealing is on the order of 1 $\mu m^2/s$, making bulk diffusion negligible. The evaporation rate is 0.1 nm/min, much smaller than the 5-35 nm/min normal surface speed experienced by surface diffusion [28]. Arguments in scaling remove evaporation and condensation from major consideration for the main factor in surface evolution [14]. Mullins describes the normal velocity as

$$V_n = \frac{D_s \gamma \Omega^2 \nu}{kT} \frac{\partial^2 K}{\partial s^2} = B \frac{\partial^2 K}{\partial s^2}, \tag{3}$$

where V_n is the velocity of the surface in the normal direction, which is proportional to the second derivative of the curvature K along the surface, D_s the surface diffusion coefficient, γ the surface free energy per area, Ω volume per atom, and v the number of atoms per unit area. A visual description is seen in Figure 7.

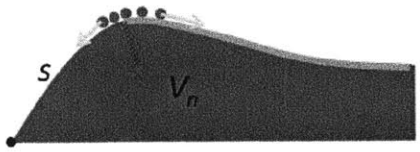

Figure 7. How surface diffusion affects curvature [14].

To arrive at the same curvature, Sudoh argues that evaporation and condensation scales by the square root of time, while surface diffusion scales by the quarter root of time, which is what is found experimentally (see Figure 8) [14].

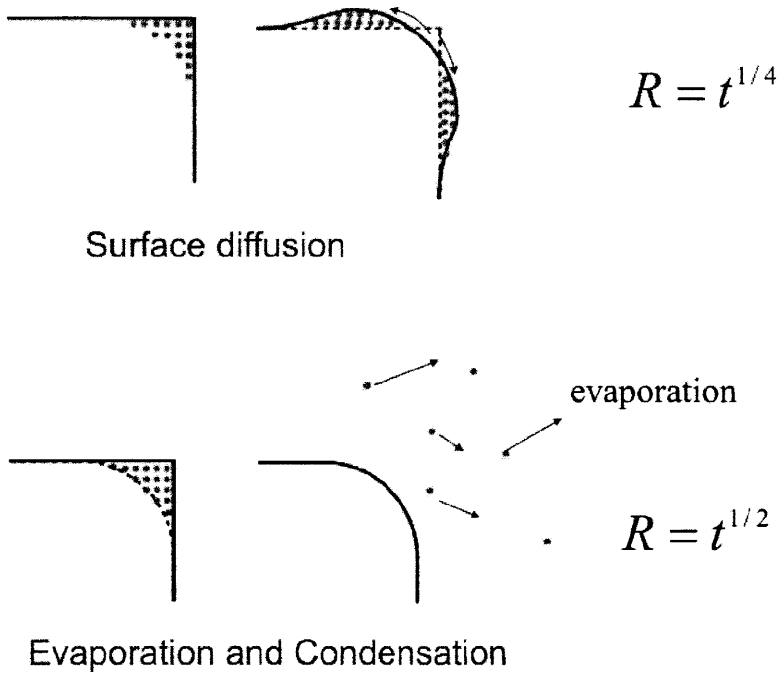

Figure 8. Mechanisms for evaporation and condensation and surface diffusion with scaling factors [14].

Herring discusses high temperature shape transformation and scalar dependence on possible mechanisms for surface evolution by using a linear dimension λ to compare the time intervals required achieve geometrically similar changes in two different, but similarly scaled grains (i.e. $R_2=\lambda R_1$). For evaporation and condensation, the scalar dependence is associated with mass transfer, the radii of curvature of the grains, and the equilibrium vapor pressure. Herring gives the rate from grain 1 to grain 2 as:

$$\text{Rate } (1\rightarrow 2) - \text{Rate } (2\rightarrow 1) \propto dS_a dS_b (p_a - p_b)/r_{ab}^2 \qquad (4)$$

Since grain 1 would have to have λ^3 the mass needed to be geometrically similar to grain 2 and the time for grain 2 to undergo this change would be a quadratic scale:

$$\Delta t_2=\Delta t_1\lambda^3/\lambda=\lambda^2\Delta t_1 \quad (5)$$

Volume diffusion, the act of atoms in a material moving through a lattice, is proportional to the local gradient o the chemical potential of the diffusing material. The chemical potential (associated with mass, e.g. λ^3) and flux (associated with contact area, e.g. λ^2) between the two grains is related by:

$$(\text{chemical potential})_2=(\text{chemical potential})_1/\lambda \quad (6)$$

$$(\text{flux})_2=(\text{flux})_1/\lambda \quad (7)$$

Thus, a cubic relationship results:

$$\Delta t_2=(\lambda^3/\lambda)*(\lambda^2/\lambda)\,\Delta t_1=\lambda^3\Delta t_1 \quad (8)$$

Surface diffusion is similar to volume diffusion, except that it occurs along a length, and (7) changes to:

$$\Delta t_2=(\lambda^3/\lambda)*(\lambda^2/\lambda)*\lambda\,\Delta t_1=\lambda^4\Delta t_1 \quad (9)$$

Herring, therefore, predicts surface diffusion to have the largest impact on shape transformation at high temperatures, with the assumption that surface energy decreases as grains grow together into an energetically favorable state [12]. Hence, changes in surface energy, the difference between energy between the surface and bulk of the material, drive surface evolution.

This background and numerous findings indicate that surface diffusion is the primary means for shape transformation in micro and nano structures fabricated on substrate surfaces at high temperatures (discussed subsequently).

Section 3.4. Surface Diffusion of Silicon in Various Environments

Researchers at Cornell University developed periodic step arrays under ultra-high vacuum (UHV) conditions to highlight the surface diffusion dominated profile decay defined by Mullins' 1957 work [17]. They determined the diffusion constant to be $0.1\exp(-2.3\ eV/k_BT)$, where k_B is the Boltzmann constant. Figure 9 displays pre- and post- annealed microchannels.

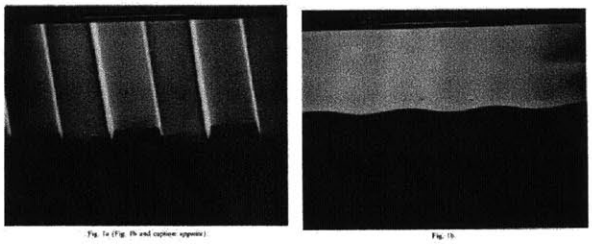

Figure 9: SEM image of 5 micron gratings via optical lithography (left). 5 micron gratings after annealing in UHV for 95 hours at 900°C (right) [17].

In other environments, different partial pressures of ambient hydrogen affect the rate of shape transformation. A forming gas of nitrogen and hydrogen is used to prevent unintended oxidation of the silicon surfaces. Although the surface diffusion coefficient is independent of partial pressure, it is hypothesized that hydrogen prevents surface diffusion by increasing the energy barrier for the diffusion of Si atoms – increasing the hydrogen pressure, therefore, lowers the rate of surface diffusion. Figure 10 demonstrates this phenomenon [18].

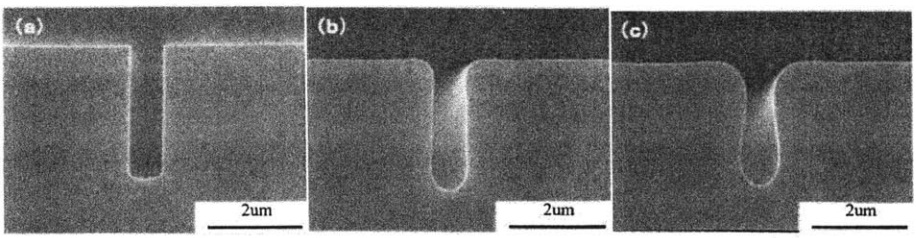

Figure 10: From left to right – 300 Torr ambient hydrogen for 3 min at 1000°; 100 Torr ambient hydrogen for 3 min at 1000°, 40 Torr ambient hydrogen for 3 min at 1000° [18].

One group of researchers investigated methods to develop a process to fabricate sinusoidal structures for electronic and optical semiconductor applications which would otherwise be difficult to replicate using traditional micro-manufacturing techniques. Using Atomic Force Microscopy, the researchers concluded that surface diffusion was the dominant mass transport mechanism due to the $1/L^4$ scaling dependence of decay as described by Mullins, where L is the wavelength of the sinusoidal curve. Figure 11 summarizes these results [19].

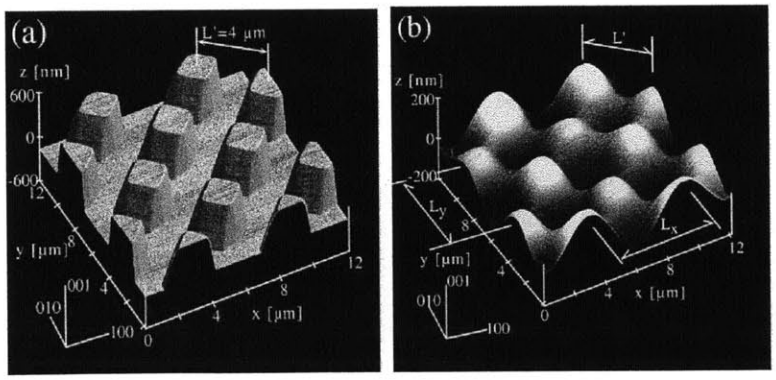

Figure 11: Atomic Force Microscope (AFM) image of 550 nm structures 4 microns apart(left). After annealing in UHV for 60 min at 1100° C (right) [19].

One potential solution to the surface diffusion phenomenon is the use of a diffusion barrier, which is a micron thick layer of metal or ceramic to prevent the movement of atoms. Titanium nitride (TiN) is an important component in the semiconductor industry, preventing diffusion of metals into regions of silicon. Its good electrical conductance and inertness makes it favorable for improving transistor performance. Titanium nitride is deposited through sputtering, a thin-film deposition technique that utilizes ejected plasma [20]. In a study by Schlemmer, et al, hafnium oxide was used to hinder surface diffusion on tungsten, and future work from this investigation hopes to mirror their success [21].

Chapter 4: Surface Diffusion Experimental Design

Section 4.1. Surface Diffusion Simulation Model

The simulation code (see Appendix A.2), developed by Stephen Bathurst, Ph.D Candidate 2011, models the surface evolution by the Mullins equation for surface diffusion, namely

$$V_n = \frac{D_s \gamma \Omega^2 \nu}{kT} \frac{\partial^2 K}{\partial s^2} = B \frac{\partial^2 K}{\partial s^2}. \tag{10}$$

Different materials can be used if the surface diffusion constant is known. As mentioned in the previous section, the variables are highly dependent on temperature and pressure conditions [16]. Figure 12 compares the shape evolution between experimental and simulated results using Mullins' equation [14].

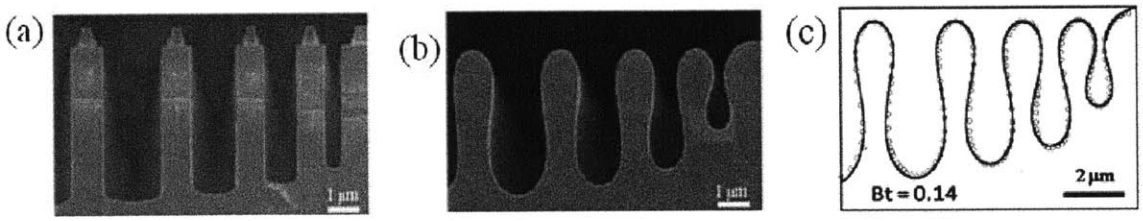

Figure 12. SEM images showing (a) Initial trench array, (b) Structure after annealing under 4% H_2/Ar ambient at 760 Torr and 1150° C conditions for 5 mins (c) Simulated profile [14].

In the MATLAB simulation model, the surface geometry is described in nodes, evolving over time based on the approximated second derivative of the curvature. Each point has a space name, x and y coordinates, curvature, normal angle, and velocity. By describing the points in space and tracking their movement over time in this manner, new frames can be calculated with each loop. Here, the frames are equivalent to 1 second. However, in the

experimental analysis, a more accurate time measure will be determined. The model is capable of converting a comma-separated file of surface profile coordinates into MATLAB code, allowing for facilitated profile processing. Figure 13 is a grating in tungsten at 1000 °C for 1, 10, and 100 hours, according to the simulation.

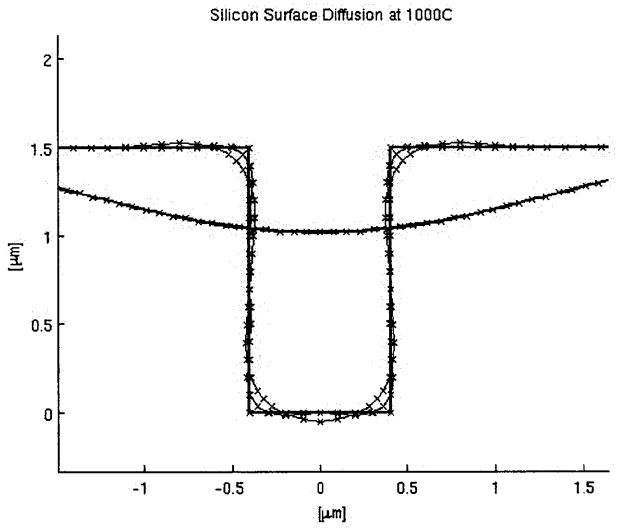

Figure 13: Evolution of tungsten at 1000 °C for est. 1, 10, and 100 hours.

Section 4.2. Microchannel Fabrication

Chip manufacturing took place at Microsystems Technology Laboratories (MTL) using the dicing machine. Due to the prohibitive cost of tungsten, silicon was chosen as an economical and adequate substrate for this investigation. To develop multiple channel surfaces, chemical etching[2] and deep reactive-ion etching were proposed. These practices, although standard practices in the field of MEMS technology, require training and costs beyond the scope of this study. Therefore, the alternative solution proposed was to utilize a dicing machine with diamond

[2] A chemical etch procedure for silicon substrates is presented in Appendix I

saw blades to cut multiple 10 mm by 10 mm squares of a 500 micron thick silicon wafer and to manually notch channels (see Figure 14). The channels were made by just touching the blade to the surface. A scanning electron microscope (SEM) image is presented in Figure 15.

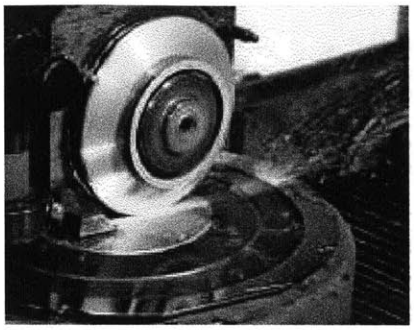

Figure 14: Dicing Blade cutting a silicon sample [25].

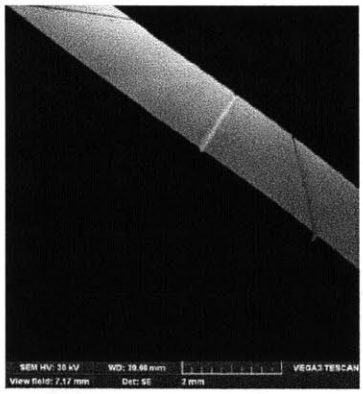

Figure 15: SEM image of fabricated microchannels

Section 4.3. Surface Characterization

Originally, the channel profiles were taken with a white light interferometer. As Figure 17 demonstrates, the incompleteness in the surface profile is due to the steepness of the vertical sides of the channel walls. The light scattered away from the lens and the Zygo Optical Profilometer (see Figure 16) was unable to measure the entire feature (see Figure 17). More importantly, the corner feature was not imaged fully, so the curvature change over time cannot

be determined to fit against the simulation model. Therefore, the pre-annealed and post-annealed surface features of the silicon samples were measured by the DekTak Profilometer, which uses contact profilometry with a 12.5 micron thick stylus to measure the changes in step height of the substrate (see Figure 18).

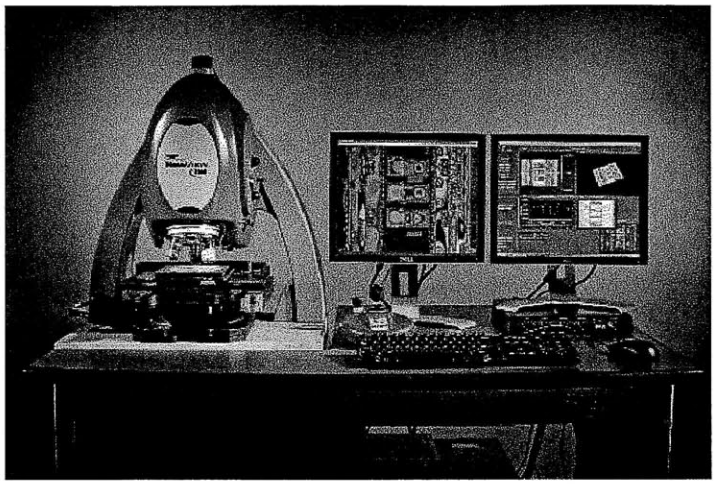

Figure 16: Zygo White Light Interferometer [26].

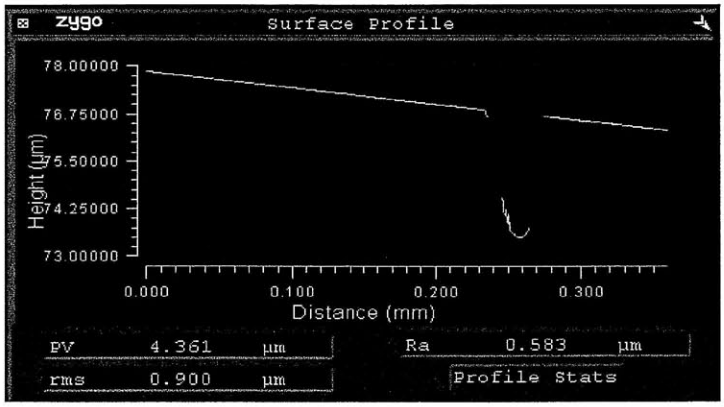

Figure 17: Incomplete surface profile.

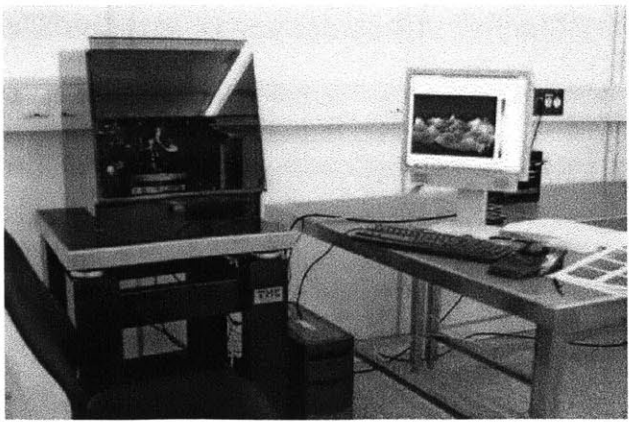

Figure 18: DekTak Contact Profilometer [27].

Section 4.4. High Temperature Annealing

The samples were heated at 900° C for 10 hours under 95% nitrogen and 5% hydrogen (38 torr partial pressure) forming gas conditions. After failing to distinguish surface evolution on the silicon samples after annealing, the samples were annealed at a higher temperature 1100° C for 7 hours under similar ambient conditions. The samples are placed in a quartz "boat," a special, high temperature vessel that can withstand the high temperatures. Temperature is ramped at a rate no faster than 50 °C/min, for proper temperature readings. After annealing, the samples are allowed to be cooled for handling. Under most high temperature annealing procedures, a thorough clean of the wafer is necessary to remove any organic material that may affect the features of the samples.

Chapter 5: Results and Discussion

Section 5.1. Results

The following contact profilometry scans were taken after 7 hours of annealing at 1100 °C. The first plot is the original plot. The second and third plots are post-annealing characterizations (Figure 19). Figure 20 is the before and after profilometry on the same plot with curvatures added. Note the scaling in Figure 20 is used to highlight the curvature, 50 pixels:5 microns for the vertical dimension and 50 pixels:20 microns for the horizontal dimension. The curvature was determined by the horizontal scaling of the plot, which would be an overestimation since the scale is more sensitive to horizontally. The curvature on the left side is compared against the simulated results. It is predicted that there is inherent hysteresis in the stylus, so the first curvature should be more accurate than the second curvature, since the stylus must be dragged along the bottom of the trench before resurfacing. Since the stylus radius is 12.5 microns, surface roughness smaller than this value cannot be detected. From these plots, it is clear that surface diffusion has taken place, based on the background chapters 3 and 4. Table 1 summarizes the results and properties during the annealing process. Simulated results are shown in Figure 21.

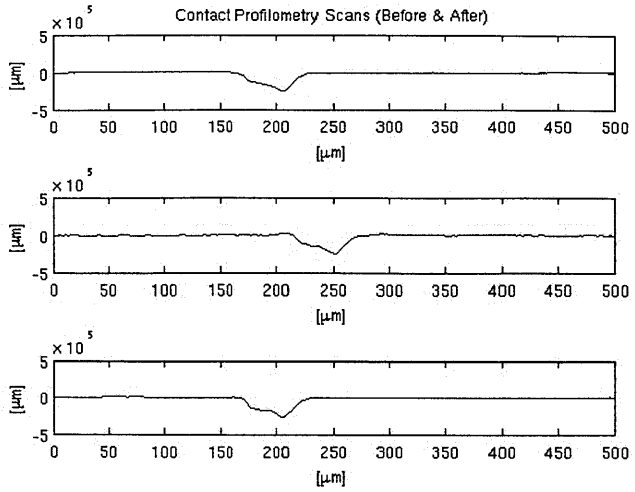

Figure 19: Pre-annealed, original surface characterization (top), Post-annealed surface characterization, Trial 1 (middle), Post-annealed surface characterization, Trial 2 (bottom).

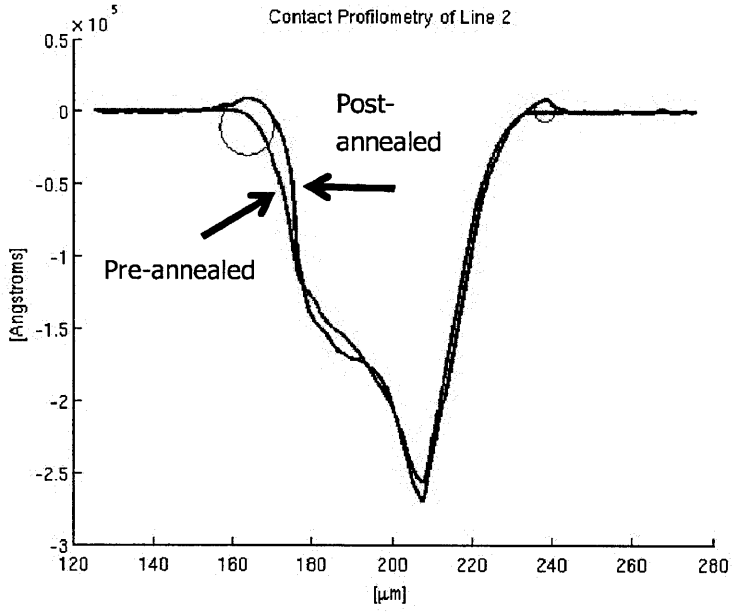

Figure 20: Pre-annealed (red) and post-annealed (blue) profiles with radius of curvature.

Channel depth	25.9 microns
Scale	50 pixels:20 microns
Radius of curvature 1	0.111 1/μm
Radius of curvature 2	0.3125 1/μm
Radius of curvature (simulated)	0.0.0833 1/μm
Annealing Temperature	1373.15 K
Surface Diffusion Constant D_s	$6.5 \cdot 10^{-8}$ cm^2 [28]
Surface Energy per Area γ	1230 dynes/cm [28]
Volume per Atom Ω	$2.0 \cdot 10^{-23}$ cm^3/atom [28]
Surface Atom Concentration	$3.448 \cdot 10^{-16}$ cm^2/atom [28]

Table 1: Surface profile characteristics and silicon properties

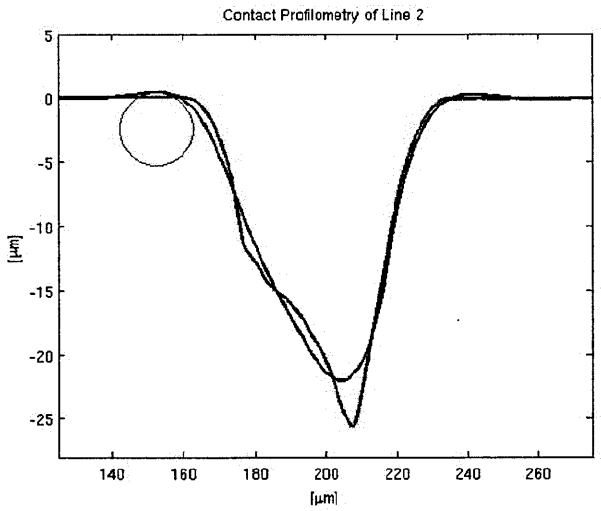

Figure 21: Simulated profile (black) compared to original profile (red).

Section 5.2. Discussion

In terms of corner rounding, the model has the capacity to agree with the actual curvature determined during experimentation, to the first order. However, many aspects of the experimental and simulated results must be scrutinized for an objective analysis of the undertaken procedures.

Section 5.3. Time scaling

As mentioned previously in Chapter 4, one frame in the MATLAB code loop is equivalent to one second. Therefore, 25,000 frames, as was used for the simulation, is equivalent to 7 hours corresponding to the annealing time of the sample. However, from the experimentation in [28], significant changes in curvature occurred in a short period of time under similar annealing conditions. Figure 22 demonstrates such an occurrence.

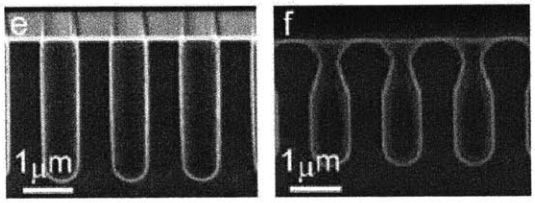

Figure 22: Pre-annealed 1.8 micron features (left). Post-annealed features at 1100° C, 60 Torr for 10 min (right) [28].

Curvature that dramatic would suggest that one frame in the MATLAB code would result in each frame being fractions of a second. How to correlate frames with time hinges on the variable "time_step" in the MATLAB code, in which the product of the incremental step in time and velocity vector changes the x- and y- coordinates of the plot. The time step cannot be too large, or the simulation falls apart due to the large changes in curvatures leading to singularities. Presumably, the total time would be the product of the number of frames and the time step. However, this leads to a total annealing time of 5000 hours, which is not only inaccurate but also unreasonable. Correlating the time step to the actual rate of surface diffusion would be the next step in validating the model.

Section 5.4. Trench Feature Discrepancy

From the simulation model, the bottom of the channel trench moves upwards, and the trench becomes shallower. However, the experimental data suggests that there is little to no change in channel depth. The literature demonstrates both of these phenomena, with one (Figure 9) suggesting the channel depth diminishes to a flat, gently sinusoidal surface and one (Figure 22) suggesting the channel depth remains the same. The difference between the two examples is the aspect ratio of the trenches- depth to width ratio of Figure 9 (from Keeffe) was 1:5 while the one for Figure 22 (from Sudoh) was 4:1. Since the experimental trench had an aspect ratio of 3:1, it is expected that it would exhibit behavior like Figure 22, in which the channel depth does not change as drastically. Another key difference between Figures 9 and 22 is the duration of annealing. Figure 6 took place for 100 hours while Figure 22 took place for 10 minutes. Since the MATLAB simulation modeled the trench becoming flatter, it may imply that the model predicts geometries with annealing under longer annealing times, which is not accurately. Ergo, even if the desired simulation is for geometries after 7 hours of annealing, the actual simulation is for annealing after much longer than 7 hours of annealing. Again, this divergence would be an issue with the time scale of the model. The time scale would also affect the velocity at specific moments in time, and the errors may be exaggerated at the trench profile. Therefore, the simulation model might not capture this phenomenon of changing trench depth of various aspect ratios accurately.

Section 5.5. Overall Degree of Surface Diffusion

Despite high temperature annealing for 7 hours, the degree of the change in curvature characteristic of surface diffusion is low. Under comparable annealing conditions, many

examples in the literature indicate a high degree of curvature in times as short as 3 minutes. A handful of theories will be discusses subsequently.

It is possible that the forming gas was not effective in preventing oxygen into the annealing chamber, causing thermal oxidation and a layer of silicon dioxide to form on the sample. This oxide layer would hinder surface diffusion from occurring, potentially to the degree seen in experimentation.

The literature provides precision driven features on the 1 micron scale. While cheaper and less time intensive, the rudimentary channel fabricated features might have inhibited surface diffusion from taking place, such as rough, rounded corners or features that were too large (on the 60 micron scale). It is possible that surface diffusion is not as dominant when the geometries are too large. Therefore, a much longer annealing time would be necessary to see significant changes in curvature at this scale.

One effect that has been well documented is the effect of hydrogen adsorption in decreasing surface evolution. The discrepancy between high temperature annealing under ambient hydrogen conditions and ultra high vacuum conditions lies on hydrogen's termination of the silicon surface suppressing the surface diffusion of silicon surface atoms (also known as adatoms)[28]. The adsorption and desorption of hydrogen atoms affects adatom diffusion, since the rate determining process is the hydrogen's release from a given configuration on the silicon surface. The surface atom moves to the most stable configuration and then moves to a site with a hydrogen atom, displacing it in the process with enough molecular energy. Once the adatom arrives at the next stable configuration, another hydrogen is adsorbed to the surface. A hydrogenated dimer (structurally similar molecular units) functions as a blockade for silicon surface diffusion along the line of motion. The increase in the diffusion energy barrier is

therefore the result of the high stability of the most stable geometric configuration, corresponding to an energy barrier to diffusion [29].

Molecular hydrogen from silicon surfaces adsorbs and desorbs via first-order kinetics, meaning that the reaction only depends on the concentration of hydrogen. Barriers to adsorption include achieving activation energy as well as having a favorable, geometric configuration with favorable adsorption trajectories and favorable surface atom motion. When the surface temperature is increased, adsorption increases, correlating to a higher sticking coefficient, which is used to quantify adsorption. This phenomenon indicates that hydrogen adsorption onto the silicon surface is activated at elevated surface temperatures and increased molecular energy. Translational and vibrational degrees of freedom, as well as lattice excitations greatly promote adsorption, decreasing the ability for silicon adatoms to migrate and inhibiting surface diffusion [30].

Chapter 6. Conclusion

The surface diffusion simulation model provided a good first-order approximation of the changing curvatures expected under high temperature annealing. Silicon samples were cut with a traditional dicing machine, which also manually created microchannels for surface profile characterization. After annealing, surface diffusion was prominent by characteristic changes in curvature. Simulated and experimental results were within 25% of each other (0.0833 1/μm vs. 0.111 1/μm, respectively). Many parameters, such as hydrogen adsorption's effect on silicon surface energy, time and geometry scales, and experimental procedure, were explored for potential causes of simulated discrepancies. The time step especially had inherent variability that affected the accuracy of the model. Future work will focus on using accurate time scales for simulation modeling.

Thermophotovoltaic systems have the ability to make great contributions towards the goal of achieving energy independence and diversification. In order for TPV to become a viable alternative energy solution, continuing research in thermal stability of selective emitters is necessary. In particular, achieving thermal stability of selective emitters will raise overall performance by increasing the spectral emissivity of such TPV technologies. The development of effective diffusion barriers, along with nano-structured features, can progress selective emitter design and applications, with the ultimate goal of producing scalable and cost-effective TPV systems for a world run by alternative energy systems.

Appendix

Section A.1. Anisotropic Chemical Etching Procedure

Etching of silicon wafers is a commonplace procedure in the semiconductor research community. However, there are several time and chemical sensitive steps necessary for the successful completion of anisotropic chemical etching. The first step is to create a thermal oxide layer on the silicon wafer. This consists of a thorough chemical cleaning of the wafer to remove impurities on the surface and firing the wafer to temperatures of 1200 degrees C. The thickness is time dependent. Photoresist, a photolithography material, is layered onto the wafer, usually through a spincoating process. This layer is partially baked and then covered in a lithography mask while UV light cures the unexposed photoresist. Depending on a positive or negative photoresist, the uncured or cured solution, respectively, are removed with a solvent. A buffered oxide etch (BOE) using a diluted HF (hydrofluoric) acid solution or a dry plasma etch removes the silicon dioxide (oxide) layer at a rate of 700 angstroms per minute. Another solvent removes the hardened photoresist. Finally, a KOH (potassium hydroxide) etch dissolves the channel feature into the silicon wafer, typically at a rate of 1 micron per minute. This can change based on molarity of the KOH solution and temperature. It is important to note that this chemical etch is not purely anisotropic, as there is a 35.26 degree angle to the vertical [31]. Figure 23 a-e displays this process.

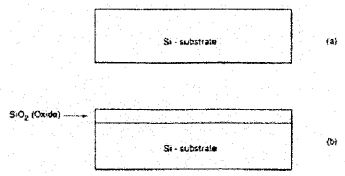

Figure 23-a: Thermal oxide layer [31].

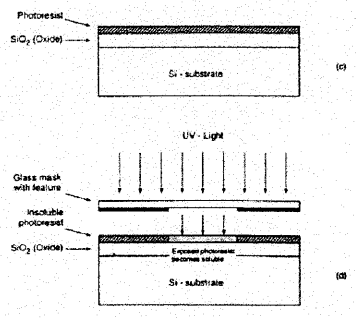

Figure 23-b: Partial photoresist bake and UV treatment [31].

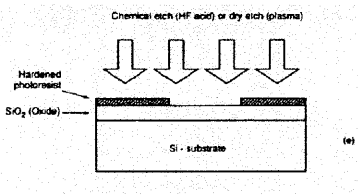

Figure 23-c: BOF chemical etch of oxide [31].

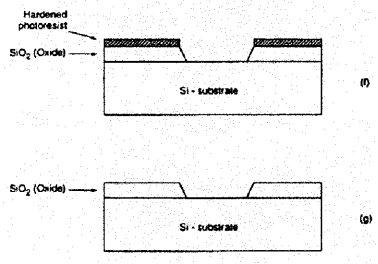

Figure 23-d: Remaining Photoresist Removal [31].

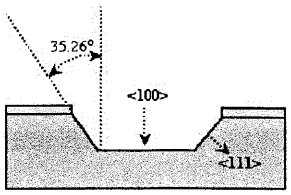

Figure 23-e: KOH etch of silicon [31].

Section A.2. MATLAB .m-code for Surface Diffusion Modeling

```
% Developed by Stephen Bathurst, 2011 Candidate in Ph. D in Mechanical
% Engineering
tic;clear all;close all;

clear all
close all
fileToRead1='/afs/athena.mit.edu/user/s/u/sun_kim/matlab/4 Two.csv';
fileToRead2='/afs/athena.mit.edu/user/s/u/sun_kim/matlab/9 two_1.csv';
fileToRead3='/afs/athena.mit.edu/user/s/u/sun_kim/matlab/10 two_2.csv';

DELIMITER = ',';
HEADERLINES = 19;

newData1 = importdata(fileToRead1, DELIMITER, HEADERLINES);
lateral1=newData1.data(:, 1);
um1=newData1.data(:, 2);

newData2 = importdata(fileToRead2, DELIMITER, HEADERLINES);
lateral2=newData2.data(:, 1);
um2=newData2.data(:, 2);

newData3 = importdata(fileToRead3, DELIMITER, HEADERLINES);
lateral3=newData3.data(:, 1);
um3=newData3.data(:, 2);

% subplot(3,1,1)
% plot(lateral1,um1)
% subplot(3,1,2)
% plot(lateral2,um2)
% subplot(3,1,3)
% plot(lateral3,um3)
% figure

%hold on
%smooth(lateral3);
shift=1; % [um]
left_crop=125; % [um]
left_index_1=round(length(lateral1)/max(lateral1)*left_crop);
left_index_3=round(length(lateral3)/max(lateral3)*left_crop);
right_crop=275; % [um]
right_index_1=round(length(lateral1)/max(lateral1)*right_crop);
right_index_3=round(length(lateral3)/max(lateral3)*right_crop);
plot(lateral1(left_index_1:right_index_1),um1(left_index_1:right_index_1),'r'
,'LineWidth',2)
```

```
plot(lateral3(left_index_3:right_index_3)+shift,um3(left_index_3:right_index_
3),'LineWidth',2)
title('Contact Profilometry of Line 2')
xlabel('[\mum]')
ylabel('[\mum]')

%% Inputs
T=1373.15; % K (Tempurature - input)
k=1.3806503*10^-16; % (g*cm^2) / (s^2*K*atom) (Boltzmann constant - input)
Ds=6.5*10^-8; % cm^2 / sec (1)
Gamma=1230; % dynes/cm = g/sÂ² (1)
Omega=2.0*10^-23; % cm^3 / atom (1)
% Surface area per atom
A0=3.448*10^-16; % cm^2 / atom (1)
C0=1/A0; % atoms / cm^2 (derived)
B=(Ds*Gamma*(Omega^2)*C0)/(k*T); % cm^4/sec
B=B*10^17; % [micron*10]^4/sec
%%


clear x y frame

% diameter: 704 nm
% radius: 352 nm
% period: 832 nm
% depth: 1536 nm
n=20;
x=downsample(lateral1(left_index_1:right_index_1),n);
y=downsample(um1(left_index_1:right_index_1),n)./10000;
frame(:,1)=x;
frame(:,2)=y;

scale=1;

pts=length(x);
frames=25000;
frame(:,3:4)=ones(pts,2);

%% Setup Calculation Matrices
A=sparse(diag(ones(1,pts-1),1)+diag(-2*ones(1,pts))+diag(ones(1,pts-1),-1));

ax=sparse(diag([-1 zeros(1,pts-2)],1)+diag([1 -1*ones(1,pts-
1)])+diag(ones(1,pts-1),-1));
bx=sparse(diag(ones(1,pts-1),1)-diag([ones(1,pts-1) -1])+diag([zeros(1,pts-2)
-1],-1));
cx=sparse(diag([2 ones(1,pts-2)],1)+diag([-2 zeros(1,pts-2) 2])-
diag([ones(1,pts-2) 2],-1));

ay=sparse(diag([1 zeros(1,pts-2)],1)+diag([-1 -1*ones(1,pts-
1)])+diag(ones(1,pts-1),-1));
by=sparse(diag(ones(1,pts-1),1)-diag([ones(1,pts-1) 1])+diag([zeros(1,pts-2)
1],-1));
cy=sparse(diag([0 ones(1,pts-2)],1)+diag([0 zeros(1,pts-2) 0])-
diag([ones(1,pts-2) 0],-1));


%%%
%% Frame Format
%% Label :   S |  X   Y   K   V
%% Point1:   1 |  0   0   0   0
%% Point2:   2 |  1   0   inf -inf
%% Point3:   3 |  1   1   0   0
%% etc... frame(row,col)
```

```
%% Prealocate
dx=zeros(pts,1);dy=zeros(pts,1);
l1=zeros(pts,1);l2=zeros(pts,1);l3=zeros(pts,1);
a=zeros(pts,2);b=zeros(pts,2);c=zeros(pts,2);
area=zeros(1,pts);
d2k=zeros(1,pts);ds2=zeros(1,pts);
h=zeros(1,frames);r=zeros(1,frames);fom=zeros(1,frames);


%% Start Frame Loop
for f=1:frames
    x=frame(:,1); y=frame(:,2);

    %% Record Figure of Merit Degradation
    h(f)=(max(y)-min(y))/scale;
    r(f)=mean(x)/scale;
    fom(f)=h(f)/r(f);
    %%

    %% Calc Curvature K (col 3)
    a=[ax*x,ay*y];
    b=[bx*x,by*y];
    c=[cx*x,cy*y];
    l1=(a(:,1).^2+a(:,2).^2).^0.5;
    l2=(b(:,1).^2+b(:,2).^2).^0.5;
    l3=(c(:,1).^2+c(:,2).^2).^0.5;
    area=(b(:,1).*a(:,2)-b(:,2).*a(:,1))*0.5;
    frame(:,3)=(4.*area./(l1.*l2.*l3));
    %% Calc V (col 4)
    d2k=(A*frame(:,3));
    ds2=((l1+l2)/2).^2;
    frame(:,4)=-B*d2k./ds2;
    %% Take Time Step
    time_step=720; % [sec] 3600=1hr
    %% Calc dn vector
    dn=frame(:,4)*time_step; % [L]
    %% Calc dx vector
    dx=dn.*-c(:,2)./l3; % [L]
    %% Calc dy vector
    dy=dn.*c(:,1)./l3; % [L]
    %% Calc New X
    frame(1:pts,1)=x+dx; % [L]
    %% Calc New Y
    frame(1:pts,2)=y+dy; % [L]
    if f==1; f1=[x y]./scale;  end
    if f==10; f10=[x y]./scale; end
    if f==100; f100=[x y]./scale; end
    if f==1000; f1000=[x y]./scale; end
    if f==10000; f10000=[x y]./scale; end
    if f==20000; f20000=[x y]./scale; end
    if f==30000; f30000=[x y]./scale; end
    if f==40000; f40000=[x y]./scale; end
    if f==100000; f100000=[x y]./scale; end
    if f==400000; f400000=[x y]./scale; end

    if f==round(f/1000)*1000;

plot(lateral1(left_index_1:right_index_1),um1(left_index_1:right_index_1)./10
000,'r','LineWidth',2)

        hold on
        axis([min(f1(:,1)) max(f1(:,1)) 1.1*min(f1(:,2)) 5])
```

```
        plot(frame(1:pts,1),frame(1:pts,2),'k-','LineWidth',2);

%plot(lateral3(left_index_3:right_index_3)+shift,um3(left_index_3:right_index
_3)./10000,'LineWidth',2)
        title('Contact Profilometry of Line 2')
        xlabel('[\mum]')
        ylabel('[\mum]')
        %axis('equal')
        hold off
        drawnow
    end
end
%% End Frame Loop
%frame=[x y]./scale;

% hold on
% plot(f1(:,1),f1(:,2),'r','LineWidth',3);
%
% plot(frame(:,1),frame(:,2),'k','LineWidth',3);
%
% if f>=10;
%     plot(f10(:,1),f10(:,2),'LineWidth',1);
% end
%
% if f>=100;
%     plot(f100(:,1),f100(:,2),'LineWidth',1);
% end
%
% if f>=1000;
%     plot(f1000(:,1),f1000(:,2),'LineWidth',1);
% end
%
% if f>=10000;
%     plot(f10000(:,1),f10000(:,2),'LineWidth',1);
% end
%
% if f>=100000;
%     plot(f100000(:,1),f100000(:,2),'LineWidth',1);
% end
%
%
% %axis([-1*(1.2*max(f1(:,1))) (1.2*max(f1(:,1))) -1*(0.2*max(f1(:,2)))
(1.2*max(f1(:,2)))])
%
% xlabel('[nm]')
% ylabel('[nm]')
% time=f*time_step/3600;
% title({'Tungsten Surface Diffusion at 1200C'})
% %;['Elasped Time: ' num2str(round(time)) ' hours']})
% hold off
toc

% figure
% plot (time_step/3600:(time_step/3600):(length(h)*time_step/3600),h)
% xlabel('Normalized Time (t/t_f) []')%xlabel('Time [hours]')
% ylabel('Channel Height [nm]')
% title({'Tungsten Surface Diffusion at 1200C'})
% %;['Elasped Time: ' num2str(round(time)) ' hours']})
%
% figure
% plot (time_step/3600:(time_step/3600):(length(h)*time_step/3600),r)
% xlabel('Normalized Time (t/t_f) []')%xlabel('Time [hours]')
% ylabel('Channel Radius [nm]')
```

```
% title({'Tungsten Surface Diffusion at 1200C'})
% %;['Elasped Time: ' num2str(round(time)) ' hours']})
%
% figure
% plot (time_step/3600:(time_step/3600):(length(h)*time_step/3600),fom)
% xlabel('Normalized Time (t/t_f) []')%xlabel('Time [hours]')
% ylabel('Channel Height / Channel Radius []')
% title({'Tungsten Surface Diffusion at 1200C'})

%;['Elasped Time: ' num2str(round(time)) ' hours']})

% [1] J.P. Barbour, F.M. Charbonnier, W.W. Dolan, W.P. Byke, E.E. Martin, and
% J.K. Trolan, Â"Determination of the Surface Tension and Surface Migration
% Constants for Tungsten,Â" Physical Review, vol. 117, Mar. 1960, pp.
% 1452-1459.
```

References

1. Armstrong, R. C., and Moniz, E. J., 2006, "Report of the Energy Research Council." Massachusetts Institute of Technology, pp. 1-11, 22.
2. Molinaro, M., 2006, "What is Light?" IST 8A Lecture. University of California – Davis, pp. 1-26.
3. Celanovic, I, 2006, "Thermophotovoltaics: Shaping the Flow of Thermal Radiation." Department of Electrical Engineering and Computer Science. Massachusetts Institute of Technology, pp. 15-23.
4. Coutts, T. J., and Fitzgerald, M. C., 1998, "Thermophotovoltaics," Scientific American, 279, pp. 78-73.
5. Harder, N.-P., and Würfel, P., 2003, "Theoretical Limits of Thermophotovoltaic Solar Energy Conversion," Semiconductor Science and Technology, 18, pp. 151-157.
6. Nelson, R. E., 2003, "A Brief History of Thermophotovoltaic Development," Semiconductor Science and Technology, 18, pp. 141-143.
7. http://aerostudents.com/files/solarCells/CH5SolarCellConversionEfficiencyLimits.pdf
8. http://lees.mit.edu/lees/projects/thermophotovoltaics_project.htm
9. Gombert, A., 2003, "An Overview of TPV Emitter Technologies." Thermophotovoltaic Generation of Electricity: 5th Conference on Thermophotovoltaic Generation of Electricity. AIP Conference Proceedings, 653, pp. 123-131.
10. Bitnar, B., 2003, "Silicon, Germanium and Silicon/Germanium Photocells for Thermophotovoltaics Applications," Semiconductor Science and Technology. 18, pp. 221-227.
11. Coutts, T. J., Guazzoni, G., and Luther, J., 2003, "An Overview of the Fifth Conference on Thermophotovoltaic Generation of Electricity," Semiconductor Science and Technology. 18, pp. 144-150.
12. Herring, C., 1950, "Effect of Change of Scale on Sintering Phenomena," Journal of Applied Physics. 21, pp. 301-303.
13. http://www.keytometals.com/page.aspx?ID=CheckArticle&site=ktn&LN=PL&NM=183.
14. Sudoh, K. 2010, "Evolution of Microstructures on Silicon Substrates by Surface Diffusion," Department of Mathematics, Hokkaido University, pp. 1-26.
15. Jin, Z.H., 2011, "Surface and Boundary Energy," Computational Materials Science, Shanghai Jiaotong University, pp. 1-20.
16. Mullins, W., 1957, "Theory of Thermal Grooving," Journal of Applied Physics, 28, pp. 333-339.

17. Keeffe, M. E., Umbach, C. C., and Blakely, J. M., 1994, "Surface Self-Diffusion on Si from the Evolution of Periodic Atomic Step Arrays," Journal of Physics and Chemistry of Solids, 55, pp. 965-973.

18. Shimizu, R., Kuribayashi, H., Hiruta, R., Sudoh, K., and Iwasaki, H., 2006, "Mechanism and Control Technology of Trench Corner Rounding by Hydrogen Annealing for Highly Reliable Trench MOSFET," Proceedings of The 18th International Symposium on Power Semiconductor Devices & ICs, 2006.

19. Tanaka, S., Umbach, C. C., and Blakely, J. M., 1996, "Fabrication of Bi-Periodic Sinusoidal Structures on Silicon, Applied Physics Letters, 68, pp. 1966-1968.

20. Ting, C. Y., and Wittmer, M., 1982, "Use of Titanium-Based Contact Barrier Layers in Silicon Technology," Thin Solid Films, 96, pp. 327-345.

21. Schlemmer, C., Aschaber, J., Boerner, V., and Luther, J., 2003, "Thermal Stability of Micro-Structured Tungsten Selective Emitters," Fifth Conference on Thermophotovoltaic Generation of Electricity, AIP Conference Proceedings, 653, pp. 164-173.

22. Kang, S.-M., and Leblebici, Y., 1998, "CMOS Digital Integrated Circuits Analysis & Design," McGraw-Hill, 2, pp. 48-82.

23. Sathish Krishna, R., and Subakar, S. E., 2010, "Waste Heat Harnessing in Automobiles for On-Board Auxiliary Power Generation Using Thermophotovoltaics," IEEE International Conference on Sustaiable Energy Technologies, pp. 1-5.

24. Durisch, W., and Bitnar, B., 2010, "Novel Thin Film Thermophotovoltaic System." Solar Energy Materials and Solar Cells, 94, pp. 960-965.

25. http://www.microfab.de/foundry/services/backend/index.html.

26. http://www.micromanufacturing.com/showthread.php?t=748.

27. http://www.nbz.uni-kl.de/en/nano/analyse/dektak.html.

28. Sudoh, K., Iwasaki, H., Hiruta, R., Kuribayashi, H., and Shimizu, R., 2009, "Void Shape Evolution and Formation of Silion-on-Nothing Structures during Hydrogen Annealing of Hole Arrays on Si(001), Journal of Applied Physics, 105, pp. 1-5.

29. Jeong, S. and Oshiyama, A. 1997. "Adsorption and Diffusion of Si Adatom on Hydrogenated Si(100) Surfaces." Physical Review Letters, 79, pp. 4425-4428.

30. Kolasinski, K.W., Nessler, W., Bornscheuer, K.-H., and Hasselbrink, E. 1994. "Beam Investigations of D_2 Adsorption on Si(100): On the Importance of Lattice Excitations in the Reaction Dynamics." Journal of Chemical Physics, 101, pp. 7082-7094.

31. http://lsmwww.epfl.ch/Education/former/2002-2003/VLSIDesign/ch02/ch02.html.